



HAL
open science

Validation of boundary-layer-transition computations for a rotor with axial inflow

Kurt Kaufmann, Philip Ströer, François Richez, Caroline Lienard, Patrick Gardarein, Normann Krimmelbein, Anthony D. Gardner

► To cite this version:

Kurt Kaufmann, Philip Ströer, François Richez, Caroline Lienard, Patrick Gardarein, et al.. Validation of boundary-layer-transition computations for a rotor with axial inflow. 75th Annual Forum and Technology Display, May 2019, PHILADELPHIE, United States. hal-02907215

HAL Id: hal-02907215

<https://hal.science/hal-02907215>

Submitted on 27 Jul 2020

HAL is a multi-disciplinary open access archive for the deposit and dissemination of scientific research documents, whether they are published or not. The documents may come from teaching and research institutions in France or abroad, or from public or private research centers.

L'archive ouverte pluridisciplinaire **HAL**, est destinée au dépôt et à la diffusion de documents scientifiques de niveau recherche, publiés ou non, émanant des établissements d'enseignement et de recherche français ou étrangers, des laboratoires publics ou privés.

Validation of boundary-layer-transition computations for a rotor with axial inflow

Kurt Kaufmann
Research Scientist
German Aerospace Center (DLR)
Göttingen, Germany

Philip Ströer
Research Scientist

François Richez
Research Scientist

Caroline Lienard
Research Scientist

Patrick Gardarein
Research Scientist

The French Aerospace Lab (ONERA)
Meudon, France

Normann Krimmelbein
Research Scientist
German Aerospace Center (DLR)
Braunschweig, Germany

Anthony D. Gardner
Research Scientist
German Aerospace Center (DLR)
Göttingen, Germany

ABSTRACT

Boundary-layer-transition computations are performed using the in-house finite-volume solvers elsA by ONERA and TAU by DLR. Reynolds-averaged Navier-Stokes simulations, using the Langtry-Menter model as well as semi-empirical transition criteria, are presented using both solvers for a rotor in climb. The numerical results are compared to temperature-sensitive paint experiments conducted at DLR's rotor test facility. Concerning the Langtry-Menter computation, transition occurs with both solvers due to laminar separation close to the trailing edge, further downstream than seen in the experiment. Semi-empirical transition criteria predict transition within both codes due to laminar separation, which was not detected in the experiments. When only considering the AHD criterion, the transition locations within the numerical simulations and the experiment are in good agreement along the entire span in all three considered test cases. In addition, numerical results are presented for a test case with cyclic pitch. These unsteady boundary-layer transition computations are carried out using the semi-empirical transition criteria approach of DLR-TAU. In accordance with the static test cases, the results are promising, as long as the laminar-separation criterion is deactivated.

NOTATION

c	Chord length (m)	Re_θ	Reynolds number based on the momentum thickness
c_f	Skin friction coefficient	Tu	Turbulence intensity (%)
c_p	Pressure coefficient	$u_{x,y,z}$	Local flow velocity in x, y, z direction (m/s)
C_T	Rotor thrust coefficient	U_{inc}	Local flow velocity (m/s)
f	Pitch and rotation frequency (Hz)	x	Chordwise coordinate at a local section (m)
H_{12}	Shape factor	y	Spanwise coordinate at a local section (m)
k	turbulent kinetic energy (m^2/s^2)	z	Right-handed coordinate with x and y (m)
Λ_2	Pressure gradient parameter	γ	Langtry-Menter intermittency variable
M	Mach number	δ	Boundary-layer thickness (m)
N	Natural logarithm of (maximum) integral growth rate	δ_1	Displacement thickness (m)
N_{cr}	(Critical) transition N factor	Δ	Difference
r	Radial location (m)	θ	Momentum thickness (m)
R	Rotor radius (m)	Θ	Blade pitch angle ($^\circ$)
Re	Reynolds number based on the chord length	σ	Standard deviation
		Ψ	Azimuth angle ($^\circ$)
		y^+	Dimensionless wall distance

Presented at the Vertical Flight Society 75th Annual Forum & Technology Display, Philadelphia, Pennsylvania, May 13–16, 2019. Copyright © 2019 by AHS - The Vertical Flight Society. All rights reserved.

SUBSCRIPTS

r, tip	Referenced to the root or the tip, e.g. Θ_r
tr	Transition position
cr	Critical
t	Turbulent

ABBREVIATIONS

CF	Crossflow
TC	Test case
PD	Pressure distribution
RBT	Rotor blade transition
RTG	Rotor test facility Göttingen
TS	Tollmien-Schlichting

INTRODUCTION

Numerical computations on rotorcraft configurations often assume the flow to be fully turbulent. Nevertheless, large regions of laminar flow can appear on helicopter rotor blades in both hover and forward flight. These laminar regions have a significant impact on the helicopter performance, and fully turbulent computations tend to overestimate the power demand of the main rotor, see e.g. Dietz & Dieterich (Ref. 1).

The current approaches to boundary-layer-transition modeling for Computational Fluid Dynamics (CFD) codes face some difficult challenges when implemented into rotating systems. Significant numerical computations, including transition prediction, have been carried out on hovering helicopter rotors, e.g. Refs. 2–9. Unfortunately, helicopter rotors present a particularly difficult validation case for boundary-layer transition. The interaction of rotor trim to thrust and blade elastic model mean that the primary comparison value for many numerical studies is purely the rotor torque, which is often computed with more than 1% error, even for fully turbulent computations. However, initial studies have shown great potential for boundary-layer-transition modeling on rotors: Gardarein & Le Pape (Ref. 2) demonstrated an improvement in the power prediction for the S-76 model helicopter rotor in hover, which was also corroborated by Min et al. (Ref. 3). Sheng et al. (Ref. 4) showed a good figure of merit correlation between computations and numerical data for the full-scale tiltrotor XV-15 rotor in hover. The NASA PSP rotor data set has included boundary-layer-transition position data as well as performance data (Ref. 10), which has proven to be a more promising approach to validating boundary-layer transition prediction. Coder et al. (Ref. 5) as well as Viera et al. (Ref. 7) presented some initial work. A variety of results based on the PSP rotor data shown at the AIAA SciTech conference in 2018 (Refs. 3, 8, 9). The results barely varied in their performance prediction but they offered a wide disparity regarding the transition position prediction, showing the versatility of this approach.

Based on this background, a high-quality reference data set for a rotor in axial inflow with climb and cyclic pitch has

been acquired by Weiss et al. (Ref. 11) and Schwermer et al. (Ref. 12), respectively. This data set, acquired on the rotor test stand Göttingen (RTG) with a two-blade configuration (Ref. 12), uses a very stiff rotor and axial inflow. The resulting computations (applying a prescribed blade root angle and no structural coupling) predict the measured loads and flow phenomena well, as shown by Letzgus et al. (Ref. 13).

Investigations at DLR and ONERA have shown that approximate transition modeling in RANS (Reynolds-Averaged Navier-Stokes) simulations can provide an improved prediction of the rotor performance in hover and forward flight (Refs. 14–16) while using relatively coarse grids, which are more applicable to industrial aircraft development efforts. The GOAHEAD data set was used for validation (Refs. 17–19), but the available hot-film data is too sparsely sampled to provide reliable validation of the codes. Thus, these previous studies cannot thoroughly validate the transition models for helicopter rotor applications.

This paper will use a new, high-quality data set for climb and cyclic pitch to validate two types of transition models found in the DLR-TAU and the ONERA-elsA CFD codes: The Langtry-Menter (Ref. 20) transition transport model, based on the SST turbulence model with additional terms provides, a robust local transition prediction, which is attractive for being fully parallelisable and easily integrated into existing codes. Its disadvantage lies in the additional computation time. Integral boundary-layer methods as used by Shaw et al. (Ref. 21) as well as Zografakis et al. (Ref. 22) require an additional data structure for the line-in-flight data extraction and boundary-layer computation, but can work on very coarse meshes leading to a significant reduction in computational effort.

EXPERIMENTAL SETUP

The rotor test facility Göttingen (RTG) (Fig. 1) is a laboratory rotor facility at the DLR, which produces unsteady flow by using large cyclic pitch paired with an axial inflow (Ref. 12). For the test cases considered in this paper, the RTG uses a rigid, two-blade configuration with a radius of $R = 0.65$ m. The rotor blades comprise a DSA-9A airfoil of 9% thickness and feature a linear twist of $\Theta = -9.3^\circ$ from root to tip. The chord length of $c = 72$ mm is constant from the root up to $r/R = 0.91$, where the blades incorporate a parabolic blade tip leading to a tip chord length of 24 mm. Unsteady Kulite LQ-062 sealed gauge pressure transducers are installed at two radial positions: $r/R = 0.53$ and 0.77. The resulting flow can be well modeled by CFD for attached flow (Ref. 13), and the effect of rotational forces is sufficiently small to produce transition effects relevant for full-scale rotors (Ref. 23). The rotor can be operated without cyclic to produce a flow similar to one created by a helicopter in slowly ascending hovering flight. The wake is convected away, and ground interference avoided by mounting the rotor horizontally using a slow (< 5 m/s) wind tunnel inflow, and allowing the wake to exit the room through large ventilation doors. The boundary-layer transition position can be extracted from the pressure sensor data in cases with or without cyclic pitching, using the assumption

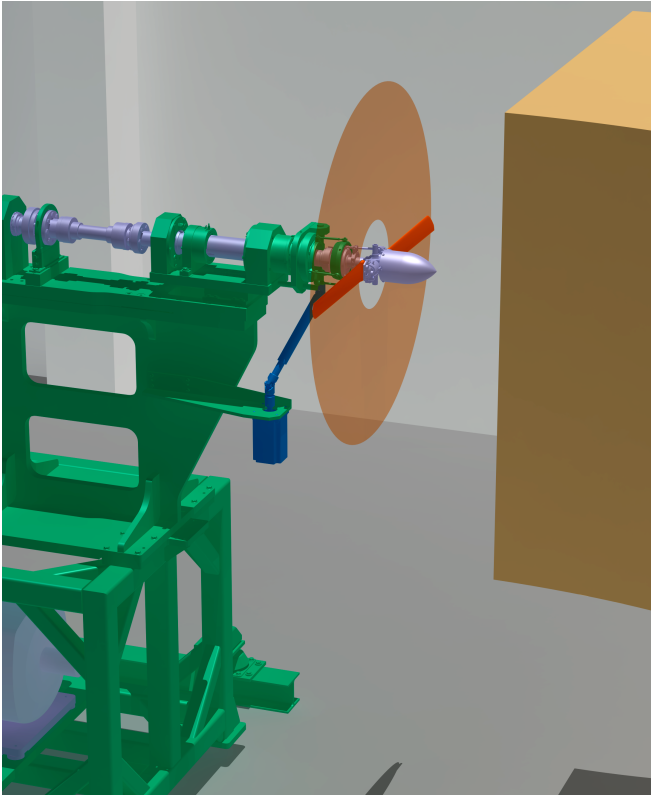


Fig. 1: The rotor test stand Göttingen (RTG) in a two-blade puller configuration after Schwermer et al. (Ref. 12).

that the motion is cyclic (Ref. 24). Additionally, Temperature Sensitive Paint (TSP) was used in cases without cyclic pitching to acquire complete surface maps of the boundary-layer transition position (Refs. 11, 23). Figure 2 shows examples of the available reference data. TSP data is available for a range of angles of attack and rotation rates, with transition points covering radial positions $r/R > 0.4$. Additionally, in the pitching test cases, the transition positions can be extracted at each of two pressure transducer radial cuts to produce hysteresis curves. The reference test cases (TCs) are listed in Table 1 and 2.

Table 1: Experimental static TCs.

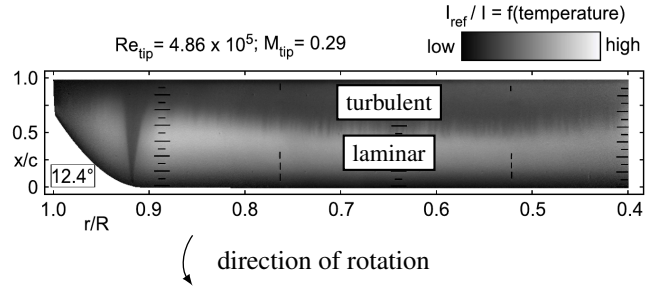
TCs	$\Theta_r(^{\circ})$	$f(\text{Hz})$	M_{tip}	Re_{tip}	u_z
TC 1	12.1	23.6	0.29	4.8×10^5	2.04
TC 2	13.1	23.6	0.29	4.8×10^5	2.08
TC 3	10.0	47.2	0.57	9.2×10^5	4.05

Table 2: Experimental unsteady TC 4.

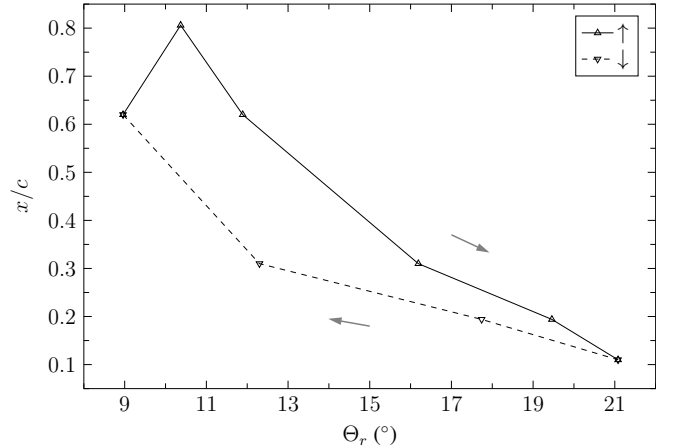
TC	$\Theta_r(^{\circ})$	$f(\text{Hz})$	M_{tip}	Re_{tip}	u_z
TC 4	$15^{\circ} + 6.1^{\circ}$	23.6	0.29	4.8×10^5	2.24

NUMERICAL SETUP

DLR and ONERA are cooperating partners on the project “Transition with rotation” to validate the transition tools avail-



(a) TSP measurement of climb test cases without cyclic after Weiss et al. (Ref. 23)



(b) Transition position from σ_{C_p} of the dynamic test case with cyclic after Schwermer et al. (Ref. 12) (TC 4)

Fig. 2: Examples of validation data for transition on the suction side.

able in the codes elsA (ONERA) and TAU (DLR). In each code, the Langtry-Menter transitional model (Ref. 20) is implemented, as well as a large number of (semi-)empirical methods such as AHD, Michel, and laminar separation. The primary tools used for semi-empirical methods comprise various transition criteria (for example Tollmien-Schlichting, laminar separation, crossflow), and report, based on which criterion boundary-layer transition occurs at each position. Then, the most upstream position is used for setting the transition position. In addition, e^N methods are available, although they are primarily used as reference data in this work.

elsA settings

The elsA solver is a CFD code (ONERA-Airbus-Safran property) that solves the compressible Navier-Stokes equations with a finite-volume approach on both structured and unstructured multiblock meshes (Ref. 25). In the present study, the structured solver of elsA is used to solve the RANS equations. Taking advantage of the rotational symmetry of the problem, the computational domain is reduced to a half cylinder around one single blade, and periodic conditions are imposed on the lateral boundaries. A farfield condition is used for the upper, lower, and external boundaries of the computational domain. A Chimera strategy is adopted. The blade grid has 5.5×10^6 points in total, with 304 points in the chord-

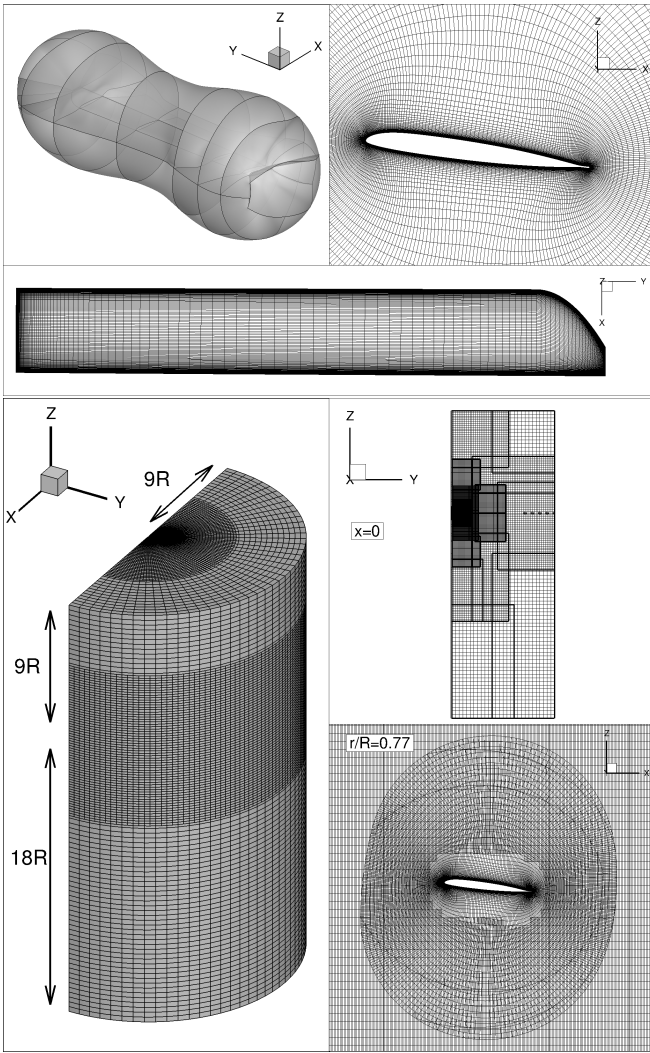


Fig. 3: elsA grid.

wise direction, including upper and lower surfaces, and 105 points in the span direction (Fig. 3). The blade grid extends up to 1.5 chords from the blade surface with 111 points in the wall-normal direction. Since transition simulations require a good resolution of the boundary layers, particular attention has been paid to the discretization in the wall-normal direction. The wall cell size, expressed in wall-unit, respects the requirement $y^+(1) < 0.5$, while at least 50 points are inside the boundary layer. The background grid is based on a 2D octree grid extruded around the rotation axis. It is composed of overlapping grid blocks of 32 million points. It extends over $9R$ above the rotor, $18R$ below the rotor and $9R$ in the radial direction (Fig. 3). The convective flux is discretized with a second-order Jameson scheme, while a second order centered scheme is used for the viscous flux. The RANS equations are formulated using the absolute velocity expressed in the rotating frame. A local time step approach with an implicit backward Euler scheme is used to reach the steady solution. At each time step, the approximate linear problem is solved applying a LUSSOR method. The grid, the numerical parameters, and the SST turbulence model (Ref. 26) are kept the same for all elsA simulations. Two transition modeling

strategies have been investigated with elsA solver. The first one is based on semi-empirical transition criteria. These criteria are computed along the wall grid line, and thus do not only depend on local parameters but also on the entire history of the boundary-layer development from the stagnation point to the local transition calculation point. Each simulation takes several criteria simultaneously to account for different transition processes, which are likely to occur. The AHD criterion is used to predict natural transition due to the growth of Tollmien-Schlichting (TS) instabilities at moderate adverse and favorable pressure gradients. The Gleyzes criterion is applied at higher adverse pressure gradients, including flow separation. Finally, the C1 criterion is used in order to address the crossflow transition process that could occur in the swept blade tip area. A detailed presentation of these transition criteria can be found in Refs. 27,28. Once the transition position is detected by one of the criteria, an intermittency value is defined on the wall and its value is set to zero for all the wall grid points located upstream of the transition and set to one for all the wall grid points located downstream. Afterwards, this wall-defined intermittency is used to weight the eddy viscosity in the 3D fluid domain following the wall-normal direction. The second transition approach uses the formulation proposed by Langtry & Menter in Ref. 20. This model defines the intermittency not only at the wall but also presents a 3D field which is obtained by solving two new transport equations. The production term of the intermittency depends on the correlation of Langtry, which is computed from local quantities. Both approaches (transition criteria and Langtry-Menter model) depend on empirical or semi-empirical criteria that drive the production of eddy viscosity. All these criteria are functions of the turbulence level. In order to investigate the sensitivity of the results with respect to this parameter, several strategies to set the turbulence levels in elsA simulations have been tested for TC 2 presented in Tab. 1.

TAU settings

DLR-TAU (Ref. 29) is an unstructured finite-volume CFD code solving the compressible Navier-Stokes equations. An implicit Euler method with a LUSGS linear solver inside a dual time stepping approach is used for the temporal discretization of the Rotor Blades Transition (RBT) simulations. The steady Langtry-Menter computations use an explicit Runge-Kutta scheme. Spatially, a second order central scheme with additional artificial matrix dissipation is used to compute the inviscid fluxes in both cases, while a Roe scheme with a second order state extrapolation is used to solve the turbulence and transition equations. For the diffusive fluxes a second order central scheme is used. The turbulence is modeled inside a RANS approach using the $k-\omega$ SST eddy viscosity model (Ref. 26).

The TAU computations use different meshes for the RBT and the Langtry-Menter approach. On the one hand, the Langtry-Menter model requires a higher resolution of the boundary layer and on the other hand, a complete two blade setup-up is needed for the unsteady computations, which are only run

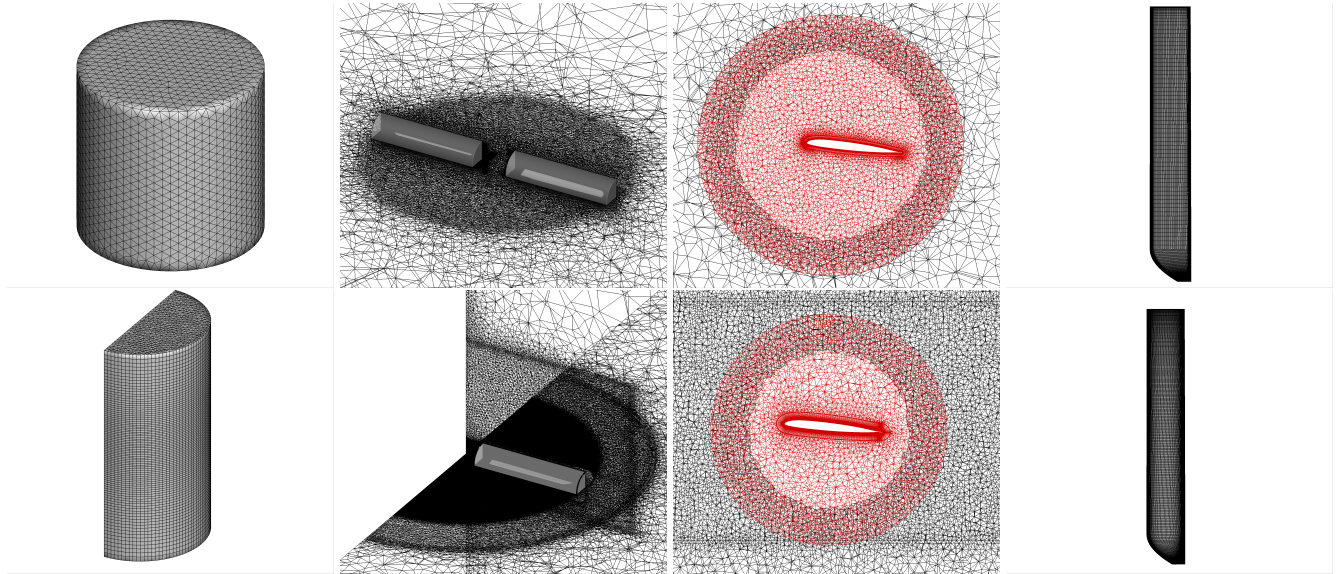


Fig. 4: Computational grid domain, chimera setup, grid sections at $r/R = 0.77$ and surface grid (from left to right) RBT mesh (top) Langtry-Menter mesh (bottom).

with the RBT tool. The two meshes are depicted in Fig. 4.

The Langtry-Menter and the RBT computations are both performed using a hybrid mesh consisting of a hexahedral grid around the blade and tetrahedral elements in the farfield. Therefore, the background farfield mesh is integrated with the blade mesh using the chimera technique. For the Langtry-Menter model, the domain can be simplified using a half-cylinder and periodic boundary conditions, given that only quasi-static climb conditions are simulated. In contrast, a complete cylinder containing both blades is used for the RBT computations, see Fig. 4 left. The primary blade mesh for Langtry-Menter computations consists of approximately 3.8×10^6 points and the overall mesh of approximately 8.6×10^6 . Each blade mesh of the RBT case comprises 1.5×10^6 points and the total mesh has 4×10^6 nodes. For both meshes, the first wall spacing was estimated considering $y^+ < 1$ for TC3. In streamwise direction, 100 points for the Langtry-Menter mesh and 120 points for the RBT mesh are used, respectively. The radial spacing is discretized with 260 points for the Langtry-Menter mesh and 100 points for the RBT mesh. The boundary-layer discretization in normal direction is ≈ 40 points for the Langtry-Menter grid and ≈ 30 points for the RBT grid.

The Langtry-Menter model is used in its original implementation as in Ref. 20 and is the same as for elsA. Accounting for the rotating frame of reference, the model was adjusted using relative velocities and corresponding gradients.

In the following section, the RBT tool, which is coupled to the DLR-TAU code, will be discussed briefly. For a more detailed description, the reader is referred to Heister et al. (Ref. 16). The RBT tool is capable of detecting five different types of transition mechanisms. The following criteria are used:

- AHD criterion (Ref. 30) for Tollmien-Schlichting (TS) transition

- Fixed shape factor H_{12} (4.029) value for Laminar Separation (LS)
- C1 criterion (Ref. 30) for Crossflow (CF) transition
- Mayle criterion (Ref. 31) for Bypass transition
- Pfenniger/Poll criterion (Ref. 32) for attachment line transition contamination

To evaluate the criteria, section cuts at 48 different radii are defined for both the pressure and the suction side. The computed transition onset positions are then used to control the turbulence model. However, the transitional region is not modeled, i.e. point transition is assumed. To compute the local turbulence level Tu , using Eq. 1, the flow velocities U_{inc} and the turbulent kinetic energy k are extracted from the (unsteady) RANS data at a user-defined distance upstream of the corresponding stagnation point.

$$Tu = 1/U_{inc} \sqrt{2/3k} \quad (1)$$

Alternatively, the user can also define the turbulence level as a global constant value (Ref. 16).

RESULTS

This section investigates the numerical computations performed on the three TCs without cyclic. The final part outlines the results of the unsteady TC with cyclic, which was computed using the DLR-TAU transition criteria method.

Static test cases

Turbulence level The turbulence intensity in the experiment was estimated by Weiss et al. (Ref. 23) using local linear stability theory and the e^N method. Firstly, the pressure distribution was computed using MSES (Ref. 33). Secondly, the

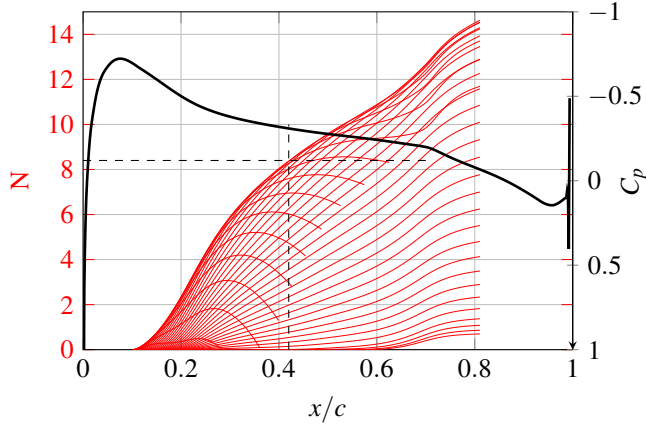


Fig. 5: Amplification of different unstable frequencies computed from laminar TAU boundary-layer profiles and estimation of the turbulence intensity based on the e^N method using the experimentally measured transition onset position.

laminar profiles were calculated by means of the boundary-layer code COCO (Ref. 34). Based on the laminar boundary-layer profiles, the stability properties were analyzed using LILO (Ref. 35). Finally, with the experimentally measured transition onset position, a critical N -factor was derived.

Figure 5 shows the amplification of different unstable frequencies computed from laminar TAU boundary-layer profiles and estimation of the turbulence intensity based on the e^N method using the experimentally measured transition onset position.

Different ways of deriving the laminar solution are compared in this work. All of them providing slightly different N -factors, however, the variation at $r/R = 0.77$ is within the experimental uncertainty:

- MSES + Coco + Lilo: $N_{cr} = 8.4 \pm 0.5$ (Weiss et al.)
- TAU + Lilo: $N_{cr} = 8.1$
- TAU + Coco + Lilo: $N_{cr} = 8.5$

Thus, according to Mack's relation, a turbulence intensity of $Tu = 0.09\%$ at $r/R = 0.77$ is assumed.

Two different strategies for turbulence level settings are available in both elsA and TAU: Either computed or prescribed global turbulence. Prescribed turbulence has a significant advantage of simplicity. Computed turbulence requires the definition of a sampling point upstream of the rotor blade leading edge, which can be difficult to define, but is theoretically also able to better treat cases where a rotor blade passes through the wake from a preceding blade or rotor head.

For the computation of the turbulence level, the DLR-TAU RBT tool uses the pressure distribution as well as the kinetic energy and the velocity vector, both extracted from the URANS solution in front of the profile sections, as an input for the transition prediction. To align with the experimental turbulence level, the kinetic energy at the far field boundary has to be set to match the extracted kinetic energy in front of

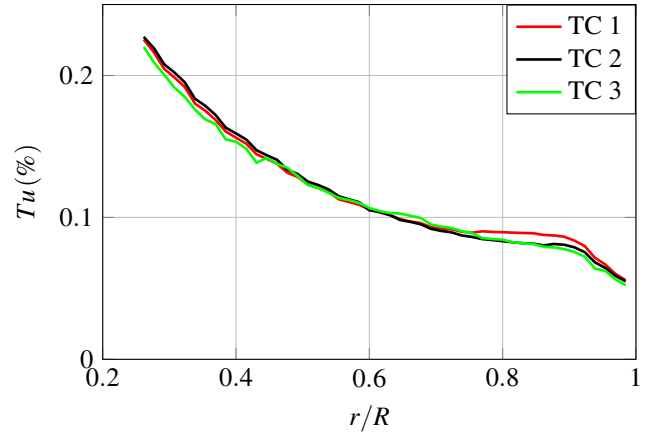


Fig. 6: Distribution of detected turbulence level at $x/c = -0.1$ over rotor radius in TAU.

the profile sections. Therefore, the sustaining turbulence concept is implemented in order to reduce the dissipation of the turbulence quantities from the farfield to the rotor (Ref. 36). For the DLR-TAU transition criteria computations, an iterative approach was conducted to match the turbulence level of $Tu = 0.09\%$ at $r/R = 0.77$. Figure 6 shows the resulting turbulence level of the three static TCs along the radial position. A decreasing turbulence level from root to tip is observed. In all three TCs, the extracted turbulence level matches $Tu = 0.09\%$ at $r/R = 0.77$.

Pressure distribution Figure 7 shows the pressure distributions of the instrumented test sections at $r/R = 0.53$ (left) and $r/R = 0.77$ (right). The pressure distributions of elsA are presented for a constant turbulence level of $Tu = 0.05\%$, whereas the TAU results are presented for the approach using Eq. 1 to calculate the turbulence level. In line 1, 3, and 5, the experimental pressure distribution is compared to the results obtained by the Langtry-Menter model for TC1, 2, and 3, respectively. Lines 2, 4, and 6 show the pressure distributions of the experiment and the computations using the transition criteria. The pressure distributions of the TAU computations match the experiment for all three TCs, both for the Langtry-Menter computations and the semi-empirical method. Although discrepancies are minor, the largest differences between TAU and experiment can be observed at the front of the pressure side at $r/R = 0.77$, where larger pressure values are present in the numerical results. Comparing the pressure distributions of the Langtry-Menter and the transition criteria approach, differences occur at the trailing edge of the sections. In the pressure distribution figure of the Langtry-Menter computations, a small suction peak is visible on the upper side at $x/c \approx 0.8$ for all TCs. This peak is a consequence of a laminar separation bubble, which occurs due to a delayed transition (discussed later). This bubble is not present in the TAU-RBT computations and thus the pressure distributions of the upper and lower side coincide when $x/c > 0.8$. The pressure distributions of elsA reveal some discrepancies when compared to the experimental data. At $r/R = 0.77$, the pressure distribution fits the experiment on the suction side, however, differences

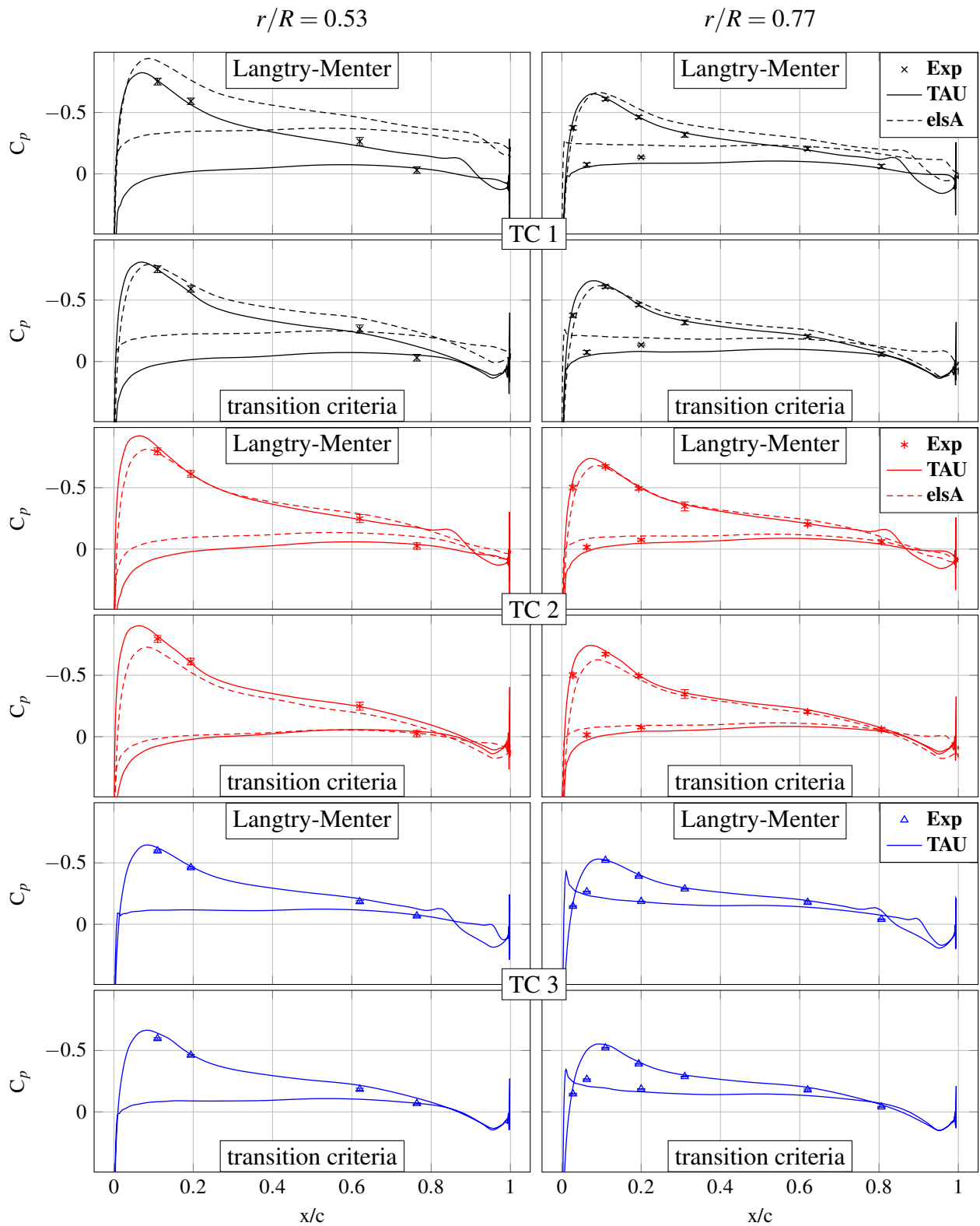


Fig. 7: Comparison of the pressure distribution for the test cases considered.

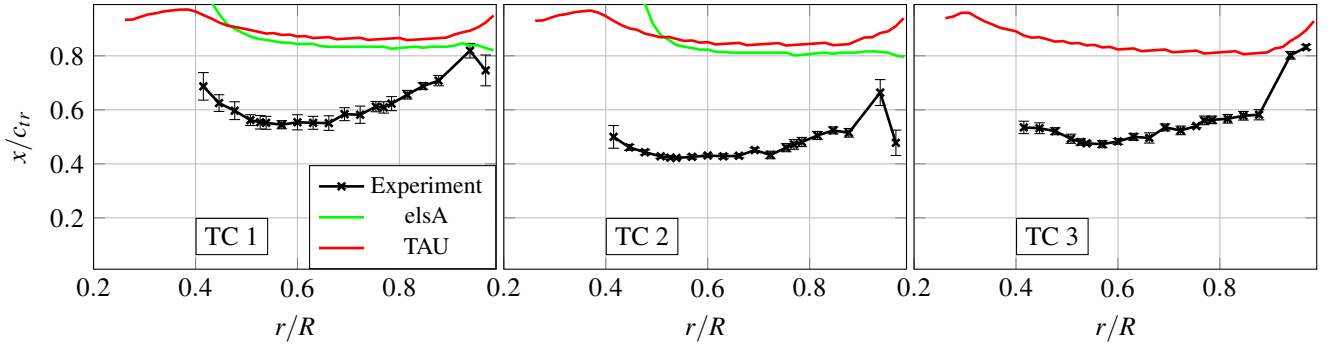


Fig. 8: Transition positions of the Langtry-Menter computations for the test cases considered.

occur on the pressure side, especially for TC1. At $r/R = 0.53$, the discrepancies are even larger. Concerning TC2, the resulting suction peak of the Langtry-Menter and transition criteria computations is lower than in the experiment. For TC1, the pressure distribution is shifted towards negative values when compared to the experiment. The TC3 computations in elsA were unstable resulting in no obtainable data.

Langtry-Menter model Figure 8 shows the transition position along the radius for the three static TCs. The transition position observed by the Langtry-Menter model is compared to the experimental transition position acquired by the TSP measurements from Weiss et al. (Ref. 23). The extraction of the transition position of the Langtry-Menter model is not straight-forward. The transition location of the Langtry-Menter TAU computations was assumed at the minimum value of the skin friction along the x -direction. This approach is justified because the flow was found to be approximately 2D (Ref. 23). In the elsA simulations, the transition position is defined as the chordwise position where the eddy viscosity ratio in the middle of the boundary layer is higher than 10 %.

For all computations using the Langtry-Menter model, transition is located in proximity to the trailing edge between $0.8 \leq x/c_{tr} \leq 1$. The TAU computations feature a bent transition distribution, and transition moves close to the trailing edge close to the root, as well as close to the tip. The most upstream transition position is observed between $0.8 \leq r/R \leq 0.9$. The transition position of the Langtry-Menter elsA computations of TC2 is comparable to the TAU case.

elsA simulations with the Langtry-Menter transition transport equation model were performed with different calculations of the turbulence level. Four simulations used a constant Tu of 0.05 %, 0.5 %, 1 %, and 1.3 % respectively. The last simulation features a turbulence level computed in each cell each cell with respect to the local value of k . As shown in Fig. 9, the transition prediction differs a lot from the experiment in all cases. In the case of the highest turbulence level ($Tu=1.3$ %), the transition starts at the blade root's trailing edge and moves progressively upstream to reach 45 % of chord at $r/R = 0.85$ and only to finally move back toward the trailing edge in the tip region. For all the other cases, the transition is located at a constant position between 80 and 85 % of chord on the main

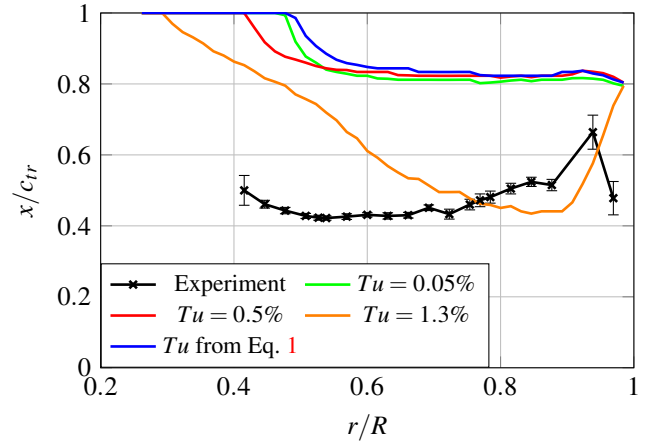


Fig. 9: elsA (Langtry-Menter model) transition position of TC 2 using different turbulence levels.

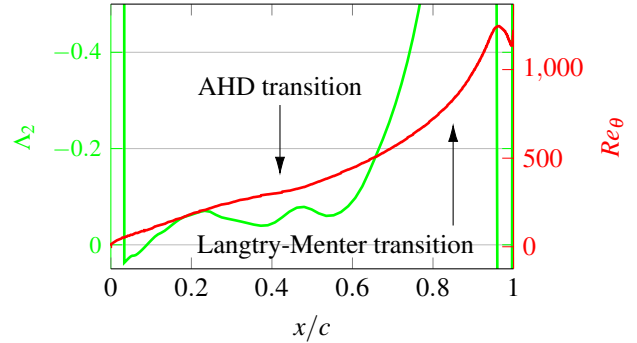


Fig. 10: elsA distribution of Λ_2 and Re_θ for TC2 at $r/R = 0.77$.

part of the blade while the flow is kept laminar up to the trailing edge of the blade root region. In each case, the Langtry-Menter transition prediction is considerably different from the experimental data and from the transition criteria results. A thorough analysis of the model behavior has shown two main deficits in the model. Firstly, the transition Reynolds number computed by the Langtry correction tends to be overestimated, especially when the adverse pressure gradient parameter Λ_2 is strong (Fig. 10). At $Tu = 0.05$ %, the Langtry correlation provides a transition Reynolds number around 900 instead of 300 for Gleyzes criterion, which leads to delayed transition.

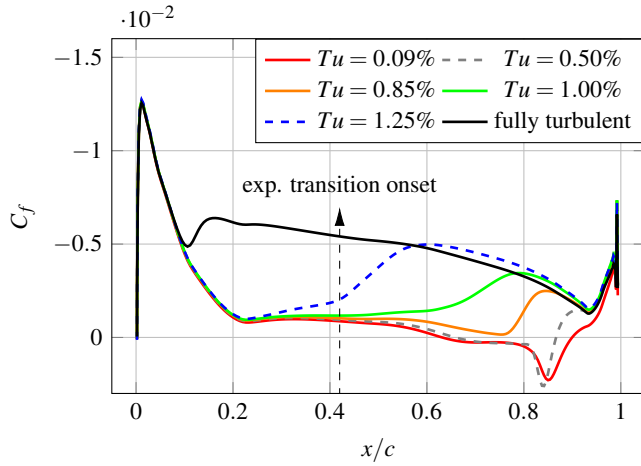


Fig. 11: C_f distribution on the suction side using 2D Langtry-Menter TAU computations with different turbulence levels. The C_p distribution is set to match the one from the 3D TAU TC2 at $r/R = 0.77$.

When the turbulence level is increased to more than 1 %, the transition Reynolds number of Langtry correlation gets lower. However, the production of intermittency is too weakly in order to provide a fast production of turbulence, which leads to a delayed transition once again.

All results obtained with the Langtry-Menter type transition models for both DLR-TAU and elsA suffer from boundary-layer transition, which occurs much too late and results in laminar separation, see Fig. 8. In order to investigate the Langtry-Menter model behavior in detail, two-dimensional computations were performed. The angle of attack in the 2D computations were set to match the pressure distribution of the experiment at $r/R = 0.77$. Figure 11 shows the C_f distribution on the suction side using the 2D Langtry-Menter TAU computations with different turbulence levels. For the estimated turbulence intensity of $Tu = 0.09\%$, compare Fig. 5, a laminar separation is present at $x/c = 0.85$. However, similar to the 3D computations, the transition is located far too downstream compared to the experiment. This corresponds with the results derived from both elsA and TAU for the full rotor (see Fig. 8 and 9). Only, an increase of the turbulence intensity up to $Tu = 1.25\%$ results in a transitional behavior close to the one of the experiment. Thus, currently it appears that the transition models must be newly calibrated for this experiment. As pointed out by Perraud et al. (Ref. 28), regarding a turbulence intensity of $Tu = 0.01\%$, the underlying criteria used inside the Langtry-Menter model overestimate the transition onset momentum loss thickness Reynolds number Re_{θ_i} for adverse pressure gradients (see Fig. 10).

Transition criteria One of the four different TAU transition criteria computations works with all five types of transition criteria, the others take only the AHD criteria into account. Investigations of Weiss et al. (Ref. 23) indicate that transition occurs due to TS instabilities in the measurement range leading to this second computation. Both computations extract values from the RANS solution and use them as an input to

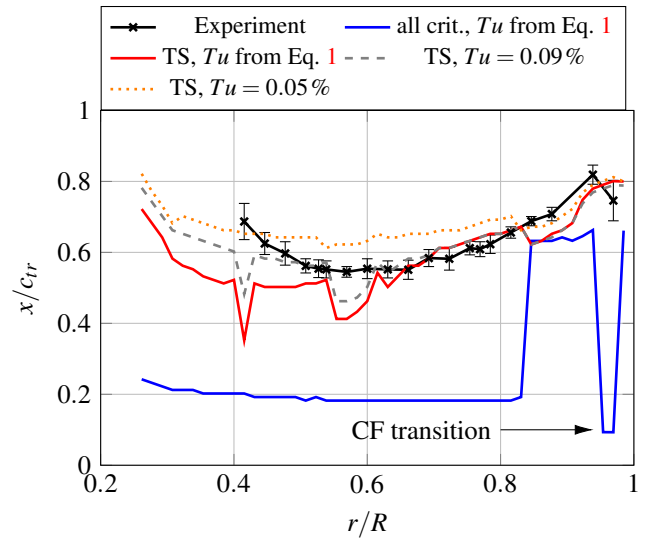


Fig. 12: Transition position along the radial position of TC1 of the TAU transition criteria computations and the experiment.

compute the turbulence intensity using Eq. 1, see Fig. 6. In addition, two computations with constant turbulence intensity of $Tu = 0.09\%$ and 0.05% as well as the AHD criterion for TS transition were carried out for comparison. Figure 12 compares the transition position of TC1 between the experimental data and the four RBT computations. The transition position detected by the TSP measurements shows a bent distribution. The most upstream transition position is located at $r/R = 0.57$ and $x/c_{tr} = 0.545$, whereas going root- and tipward, transition occurs further downstream. Utilizing all types of transition when evaluating computations in TAU, transition takes place at $x/c_{tr} \approx 0.2$ and remains almost constant between $0.3 \leq r/R \leq 0.83$. Afterwards, the transition jumps downstream to $x/c_{tr} \approx 0.63$ between $0.83 \leq r/R \leq 0.94$. From root to $r/R = 0.94$, the predicted transition type is a laminar separation bubble. However, this separation is neither present in the numerical computation nor indicated in the experimental reference study by Weiss et al. (Ref. 23). The transition of two profile sections at the tip is predicted due to CF transition.

The TS transition position predicted by the AHD criterion is more closely aligned with the experimental data. The inner part features two kinks at $r/R = 0.41$ and 0.55 , where transition is jumping upstream. The transition line is bent, and the most downstream transition point is located at the tip and the root. The kinks aside, the most upstream position is located at $r/R = 0.46$ and $x/c_{tr} = 0.50$. In comparison with the experiment, discrepancies in the transition location occur for $r/R < 0.6$, predicting the transition position of the computation more upstream than in the experiment. In case of $r/R > 0.6$, a close conformity between experiment and simulation can be observed. The computations using a constant turbulence level of $Tu = 0.09\%$ are similar to those using Eq. 1 to calculate the turbulence level. Differences occur in the center area, where for the computations using Eq. 1, larger turbulence levels are present and thus, transition occurs further upstream. At $Tu = 0.05\%$, transition appears slightly

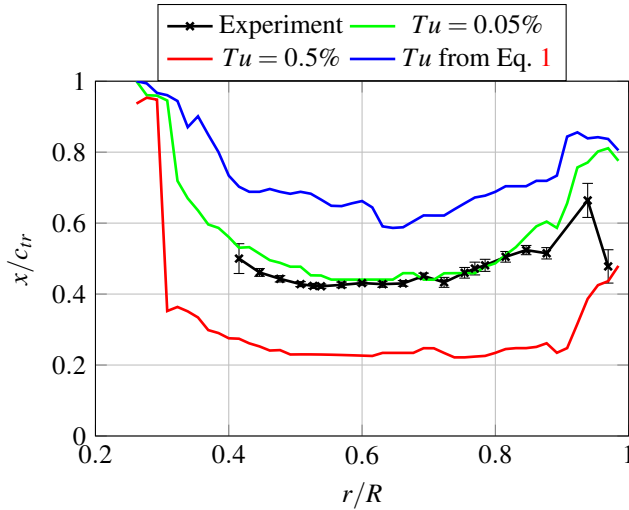


Fig. 13: elsA (transition criteria) transition position of TC1 using different turbulence levels.

further downstream compared to $Tu = 0.09\%$. Concerning this particular test setup, it can be stated that the RBT results are only acceptable, if only the TS transition criterion is used. The investigations from Weiss et al. (Ref. 23) indicated that the transition in the experiment occurs due to TS instabilities. If not stated differently, all following RBT-TAU results are obtained using only the TS transition criterion in combination with the turbulence level obtained from Eq. 1.

The influence of the turbulence level on the prediction of the transition by the criteria approach has been evaluated for the case TC2 with the elsA solver. Three numerical simulations have been performed. For two of the simulations, the turbulence level used by the transition criteria is set to a constant value of 0.05% and 0.5% respectively. In the third simulation, the turbulence level is computed locally on each streamline with respect to the local values of turbulent kinetic energy k and velocity magnitude U_{inc} taken at the edge of the boundary layer and is inserted into Eq. 1.

The transition positions obtained for these three different turbulence levels are shown in Fig. 13. The results regarding the lower constant turbulence level ($Tu = 0.05\%$) are in very close proximity to the experimental measurement. The transition is located in the middle part of the blade at around $x/c=0.45$, and moves progressively to the trailing edge in the blade tip region, which is similar to the TAU results obtained for the same turbulence level and shown in Fig. 12. At a higher turbulence level of 0.5% , the transition moves significantly upstream to reach a region located between 20% and 25% of the chord, which deviates far from the experimental data. When the turbulence level is computed locally with k , it reaches a value of around 0.03% at $r/R = 0.77$ resulting in a delayed transition.

The behavior of the transition criteria computed by the elsA code is detailed in Fig. 14, which shows the evolution of the Reynolds number based on the momentum thickness Re_θ along the section $r/R = 0.77$. Note that the AHD criterion is based on first computing the critical Reynolds number $Re_{\theta_{crit}}$,

where the laminar boundary layer is supposed to be unstable, and then computing the transition Reynolds number Re_{θ_t} , where transition occurs. These two quantities are shown in Fig. 14. When the adverse pressure gradient exceeds a set level, the AHD criterion switches to the Gleyzes criterion, which is not based on Re_θ but the N-factor N which corresponds to the growth rate of the instabilities. In this case, transition occurs when the critical value N_{crit} is reached, as given in the Mack formula. Figure 14 shows that the critical Reynolds number is first reached around 10% of chord. Then, the transition Reynolds number Re_{θ_t} is computed. At 20% of chord, Re_θ has not yet reached the transition value Re_{θ_t} , leading to the flow remaining laminar, and to the Gleyzes criterion starting to be computed. Finally, the N-factor of the Gleyzes criterion reaches the critical value N_{crit} at $x/c = 45\%$, and the intermittency function γ is set to 1 resulting in transition occurring at $Re_\theta = 350$. At a higher turbulence level of 0.5% , the transition Reynolds number Re_{θ_t} is reduced. In this case, Re_θ reaches $Re_{\theta_t} = 250$ at around 20% of chord before the Gleyzes criterion is activated.

All results obtained with the Langtry-Menter type transition models for both DLR-TAU and elsA suffer from boundary-layer transition, which occurs much too late and results in laminar separation, see Fig. 8. In order to investigate the Langtry-Menter model behavior in detail, two-dimensional computations were performed. The angle of attack in the 2D computations were set to match the pressure distribution of the 3D computation at $r/R = 0.77$. Figure 11 shows the C_f distribution on the suction side using the 2D Langtry-Menter TAU computations with different turbulence levels. For the estimated turbulence intensity of $Tu = 0.09\%$, compare Fig. 5, a laminar separation is present at $x/c = 0.85$. However, similar to the 3D computations, the transition is located far too downstream compared to the experiment. This corresponds with the results derived from both elsA and TAU for the full rotor (see Fig. 8 and 9). Only, an increase of the turbulence intensity up to $Tu = 1.25\%$ results in a transitional behavior close to the one of the experiment. As pointed out by Perraud et al. (Ref. 28), regarding a turbulence intensity of $Tu = 0.01\%$, the underlying criteria used inside the Langtry-Menter model overestimates the transition onset momentum loss thickness Reynolds number Re_{θ_t} for adverse pressure gradients (see Fig. 10).

In Fig. 15, the experimental transition position is compared to the computations using the transition criteria. elsA's transition criteria computations, using a constant value of $Tu = 0.05\%$ are shown as illustrated in Fig. 13. TAU uses the approach with a turbulence level based on Eq. 1 of the URANS solutions, see Fig. 6. In addition, only the TS transition criterion is used as illustrated in Fig. 12. Overall, the transition position of the criteria computations is in good agreement with the experiment. For TC1, the elsA computations for $r/R < 0.77$ are further downstream compared to the experiment, whereas with TAU, transition takes place further upstream than in the experiment when $r/R < 0.63$. Both computations match the experimental data in the blade tip area. The differences between the computational approaches in the center part can be

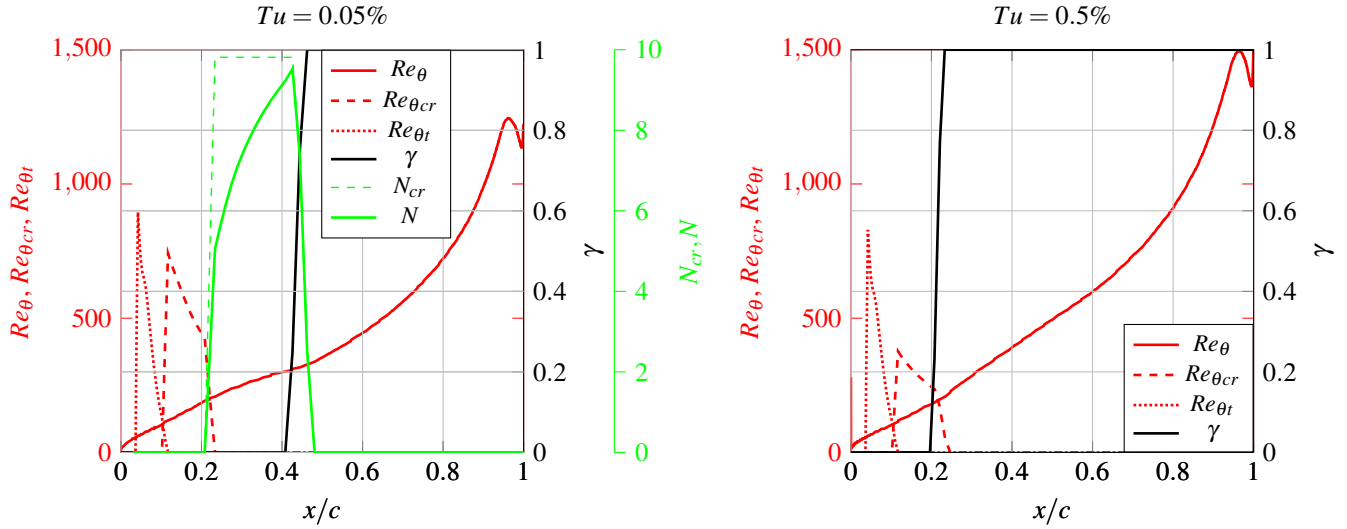


Fig. 14: Re_θ distribution of elsA at section $r/R=0.77$ using transition criteria for TC2 and different turbulence levels.

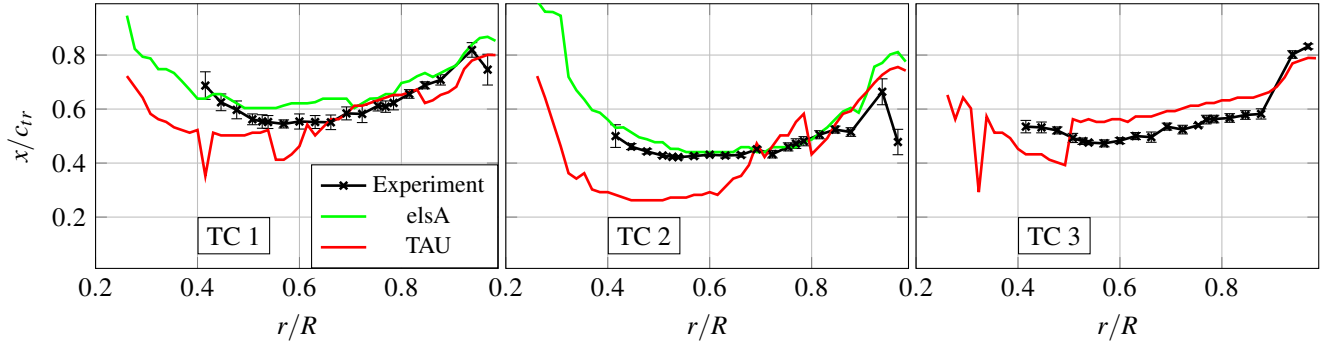


Fig. 15: Transition positions of the transition criteria computations for the test cases considered.

explained by the different treatment of the turbulence level. For TC2, the transition location of elsA fits the experimental data for the entire radius. Differences between TAU and experiment occur when $r/R < 0.67$. For TC3, TAU fits the overall transition position of the experiment with minor deviations. When $r/R < 0.5$, transition is predicted too far upstream, whereas in case of $0.5 \leq r/R \leq 0.9$ transition takes place too far downstream compared to the experiment.

The transition criteria of both elsA and TAU use an estimation of the shape factor H_{12} using a Falkner-Skan fit, which relates the pressure gradient parameter Λ_2 to H_{12} . The relation of Cliquet (Ref. 27) is used in elsA, and a mathematically equivalent method is utilized in TAU (Ref. 16). This avoids the computation of H_{12} by directly integrating data from the boundary layer (which gives a more physically correct answer), but is not used in either code due to the strict grid requirements. It appears that estimating H_{12} in this way for the helicopter airfoils and Reynolds numbers used in this study results in significant inaccuracies and an increased sensitivity of H_{12} to small changes in the pressure distribution, which is not seen for the direct computation of H_{12} .

To examine this problem, finely resolved two-dimensional simulations were conducted dealing with two slightly differ-

ent pressure distributions (PD1 and PD2), which were selected to be similar to a pressure distribution from the 3D elsA simulations. Since Weiss et al. (Ref. 11) showed that the influence of rotational forces on the laminar-turbulent transition is negligible, this simplification seems valid. Figure 16 (left) displays the resulting C_p distributions compared to the experiment.

In Fig. 16 (right), the computed shape parameters are shown. It can be seen that using the equation according to Cliquet for H_{12} as used by both codes leads to qualitatively similar results for the shape parameters computed from PD2 and the 3D pressure distribution from elsA. The H_{12} from the Cliquet equation is qualitatively different between PD1 and PD2, and the H_{12} distribution from PD1 exceeds 4, running into a limit of the Cliquet equation. This happens despite the relatively minor differences between the various input pressure distributions. In contrast, computing exact H_{12} values by directly integrating data from the boundary-layer profiles shows two effects:

1. In this case, the estimation of H_{12} using the Cliquet equation is not particularly accurate.
2. The small variation in the pressure distributions from

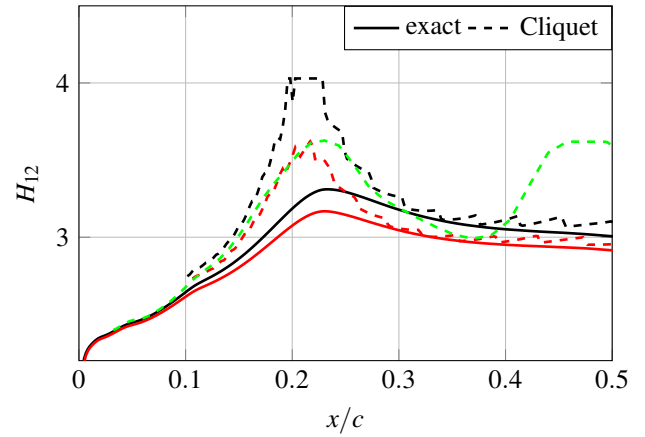
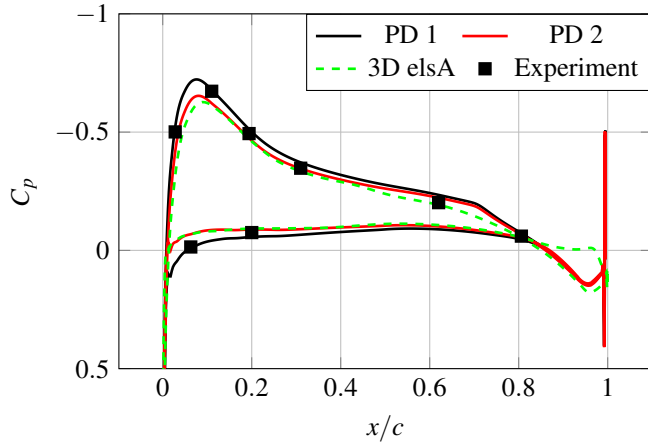


Fig. 16: Pressure distribution and shape factor for 2D TAU case.

PD1 to PD2 should result in a small variation in H_{12} , but instead the differences between the two test cases are overestimated using the Cliquet equation.

Thus, the differences in transition detection between similar pressure distributions for elsA and TAU appear to be related to the use of the Cliquet relation for the computation of H_{12} . The criteria Re_{θ_r} and consequently the transition onset position are affected due to the overestimation of the shape factor. Currently, efforts to understand and compensate for the sensitivity are underway. The transition criteria of elsA and the RBT tool of TAU also compute the momentum loss thickness θ differently, with the RBT tool using an integral method (Ref. 37) and elsA computing the momentum loss thickness exactly by integrating along the wall-normal boundary-layer profile. However, both methods result in similar θ distributions which do not appear to be the root of the observed problems. The early flow separation detection in TAU is based on a simple trigger which appears to activate incorrectly for this airfoil, and must be recalibrated or replaced with a better method.

Unsteady test case

Pitching URANS computations are performed for the TC 4, which corresponds to the fully attached TC of Schwermer et al. (Ref. 12) ($\Theta_{root}(t) = 15.0^\circ + 6.1^\circ \sin(2\pi\Omega t)$ at $\Omega = 23.6\text{Hz}$ and $u_z = 2.2\text{m/s}$, see also Tab. 2). The semi-empirical transition criteria are used with the DLR-TAU code to perform an analysis of the unsteady boundary-layer transition. The computations are run for a total of 12 revolutions. Firstly, 10 revolutions with 45 time steps per period are computed to initiate a flow field. The last two revolutions are then performed with 360 time steps per period to resolve the pitching cycle. Two computations are conducted: The first with all 5 transition criteria available in the RBT tool. The second only takes TS transition into account, compare Fig. 12. The same settings, which were applied to the static test cases, were used at the farfield, and the turbulence level was computed from the URANS solution according to Eq. 1.

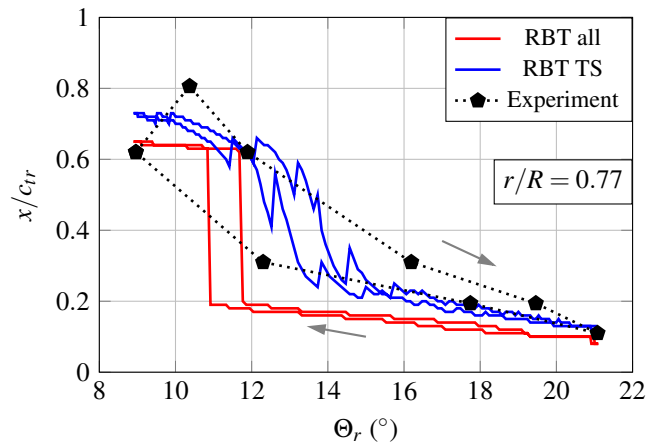


Fig. 17: Comparison of transition position on the suction side for the unsteady RBT-TAU computations with the experimental data from Schwermer et al. (Ref. 12).

Figure 17 compares the transition position over Θ_r at $r/R = 0.77$ between the experiment and the two computations performed. The experimental transition position can be extracted from the standard deviation of the pressure transducers according to Gardner et al. (Ref. 24). With this method, transition can only be detected at the instant in time when it moves across the sensor. In addition, Weiss et al. (Ref. 11) showed that the pressure transducers themselves can trigger premature transition as the pressure taps perturb the flow. This was also shown by Mertens et al. (Ref. 38) for a pitching airfoil. This effect increases with the extent of laminar flow and results in an earlier transition of $\approx 5 - 10\%$ chord. The experimental transition position moves from $x/c_{tr} = 0.11$ at $\Theta_{r,max} = 21.1^\circ$ to $x/c_{tr} = 0.81$ at $\Theta_r = 10.4^\circ$. Additionally, a hysteresis in the transition position between up- and downstroke is clearly visible. The computations using all semi-empirical transition criteria predict transition due to laminar separation, which occurs between $0.1 \leq x/c_{tr} \leq 0.2$ for $\Theta_r > 11.7^\circ \uparrow$ and for $\Theta_r > 10.9^\circ \uparrow$. At lower angles of incidence, the transition jumps downstream to $x/c_{tr} = 0.64$. As seen in the static cases, the computations, using all types of transition criteria, predict

transition which occurs further upstream compared to the experiment. The computations, which only account for TS transition, compare better with the experimental data. At $\Theta_{r,min}$, the transition is predicted at the most downstream position at $x/c_{tr} = 0.73$. Then, transition moves almost linearly upstream with increasing angle of incidence up to $\Theta_r < 13.8^\circ$, followed by a jump in the transition position from $x/c_{tr} = 0.5$ to $x/c_{tr} = 0.28$. Subsequently, a linear movement of the transition with increasing Θ_r can be observed up to $\Theta_{r,max}$. During the downstroke, only minor differences in the transition position are obtained in contrast to the upstroke for $\Theta_r > 15^\circ$. Then, a fast movement of the transition is visible at $\Theta_r < 13^\circ$. The movement is similar to that happening during the upstroke, but takes place at lower angles of incidence and thus results in a small hysteresis. In the last part of the downstroke, transition occurs only slightly further upstream compared to the upstroke. In comparison to the experimental data, good agreement is obtained with the numerical simulation using the TS transition only. During the upstroke, transition occurs more upstream in the computations, whereas during the downstroke, the numerical computations match the experimental transition position at high angles of incidence. For lower angles of incidence, transition is predicted to be further downstream than in the experiment, and the hysteresis between up- and downstroke is underpredicted by the RBT simulations compared to the experimental hysteresis.

Figure 18 shows contour plots of the transition position over the rotor disk for the two RBT-TAU computations. The computation using all types of transition criteria is shown on the top and the computation using the AHD criterion only is shown on the bottom. The suction and pressure side of the rotor blade is displayed in the left and right column, respectively.

On the suction side, for the computations using all types of transition criteria, transition occurs due to LS over the entire rotor disk, except for a narrow stripe located directly at the blade tip. Here, CF transition is detected between $15^\circ < \Psi < 165^\circ$ and causes transition up to $x/c_{tr} = 10^\circ$. Starting at Θ_{min} and $\Psi = 90^\circ$, transition occurs at $x/c_{tr} \approx 0.65$ along the entire radius, beside the tip region, where CF transition is predicted. During the upstroke, a sudden jump in the transition position from $x/c_{tr} \approx 0.65$ to $x/c_{tr} \approx 0.20$ is visible, which first occurs at the root area up to $r/R \approx 0.53$ and then extends up to $r/R \approx 0.90$. Directly at the blade tip, transition is only predicted up to $\Psi < 165^\circ$ by the CF criterion. Subsequently, the transition position is jumping downstream again to $x/c_{tr} \approx 0.65$ between $165^\circ < \Psi < 200^\circ$. At $\Psi = 270^\circ$, the most upstream transition position is reached. Transition moves slightly downstream from $x/c_{tr} \approx 0.02$ at the root to $x/c_{tr} \approx 0.12$ at the tip. The transition movement during the downstroke is comparable to the upstroke, although a small hysteresis is obtained.

For the computations taking only TS transition into account, transition occurs further downstream compared to the computations using all types of transition criteria. At Θ_{min} , transition is predicted between $0.7 < x/c_{tr} < 0.85$ along the radius. During the upstroke, a sudden upstream transition movement

is visible between $150^\circ < \Psi < 180^\circ$ from the root up to $r/R \approx 0.90$, where the transition quickly moves from $x/c_{tr} \approx 0.65$ to $x/c_{tr} \approx 0.3$. Directly at the blade tip, this movement is delayed and occurs only at $\Psi = 200^\circ$. At Θ_{max} , transition is located most upstream within the pitching cycle. From the root to $r/R \approx 0.90$, the transition is predicted at $x/c_{tr} \approx 0.1$, whereas for the tip region, transition occurs at $x/c_{tr} \approx 0.2$. Comparing up- and downstroke, only a small hysteresis in the transition position is visible, and transition occurs slightly more upstream during the downstroke compared to the upstroke.

On the pressure side, transition occurs close to the trailing edge for both types of computations. When using the computation with all types of transition, LS is detected over the entire rotor disk, except for a narrow stripe close to the blade tip, where CF transition is detected and transition moves up to $x/c_{tr} = 0.3$. Regarding the computation using the AHD criterion, the transition position is located between $0.8 < x/c_{tr} < 0.95$ for the entire angle of incidence range.

CONCLUSIONS

Investigations of boundary-layer transition in rotation were presented using RANS computations with elsA and TAU. Three test cases without cyclic have been compared to experimental validation data based on TSP measurements. The test conditions covered two rotation frequencies of 23.6Hz and 47.2Hz as well as a variation of the blade pitch angle. For both elsA and TAU, the computations are performed with a Langtry-Menter approach, and transition predictions are based on semi-empirical methods. In addition, unsteady computations with cyclic pitch were carried out and compared to experimentally derived transition positions based on the standard deviation of the pressure signal. The TAU code with the semi-empirical transition criteria approach was used for this analysis. The following conclusions can be drawn:

1. Langtry-Menter computations for both 3D and 2D suggest boundary-layer transition to be triggered by laminar separation. Transition occurs close to the trailing edge and much further downstream than in the experiment.
2. The laminar separation criteria of TAU predict boundary-layer transition further upstream compared to the experiment. However, laminar separation was found neither in the RANS solution nor the experimental reference investigation.
3. If the AHD criterion is used only for the TAU computations, the numerical transition position compares well with that from the experiment. The comparability becomes slightly worse when moving rootwards.
4. Transition is detected by the Gleyzes criterion implemented in the elsA computations. The transition position fits the experimental data very well along the entire span. Nevertheless, some discrepancies in the pressure distribution occur although the criterion was originally developed to detect laminar separation.

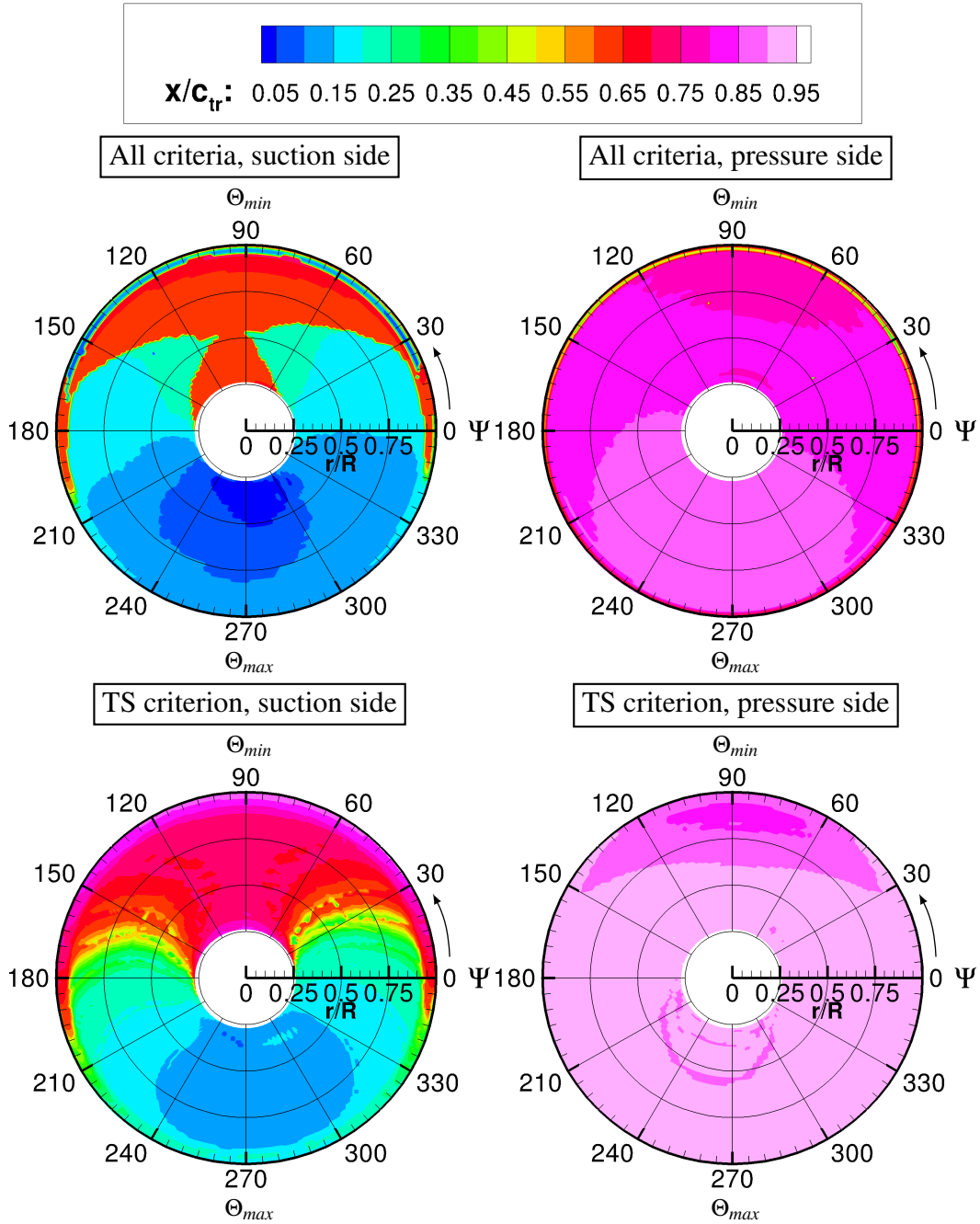


Fig. 18: Fully attached pitching case RBT prediction of laminar flow length x/c_{tr} .

5. The investigations of the boundary-layer values show that the approximated H_{12} factor is overestimated and reveal the reason for the erroneous transition prediction. The H_{12} distribution is comparable between elsA and TAU when the pressure distributions match.
6. Computations at constant turbulence levels compare better with experimental transition position than with turbulence levels computed from Eq. 1, especially in regions close to the root.
7. As in the static cases, the cyclic case exhibits boundary-layer transition further upstream compared to the experimental data. Again, the laminar separation criterion predicts transition, which is neither indicated by the experimental study nor present in the URANS data.
8. The transition location of the unsteady test case is predicted well by the computations using the AHD criterion only. Nevertheless, the computations reveal a smaller hysteresis than the experiment.

Recent optical measurements performed on the RTG allow to detect the unsteady transition movement at high spatial resolution over the entire pitching cycle, see Ref. 39. This will allow a more detailed comparison of the unsteady boundary-layer transition between computations and experiment.

ACKNOWLEDGMENTS

This work was done as part of the DLR project FAST-Rescue and the DLR-ONERA cooperation on transition with rotation. The authors gratefully acknowledge the Gauss Centre for Supercomputing e.V. (www.gauss-centre.eu) for funding this project by providing computing time on the GCS Supercomputer SuperMUC at the Leibniz Supercomputing Centre (LRZ, www.lrz.de). Valuable discussions with Beatrice Carter, Andreas Goerttler, Clemens Schwarz, Till Schwermer, and Armin Weiss are highly appreciated. Contact: kurt.kaufmann@dlr.de

REFERENCES

¹Dietz, M. and Dieterich, O., “Towards increased industrial Application of Rotor Aeroelastic CFD”, 35th European Rotorcraft Forum, Hamburg, September 22-25, 2009.

²Gardarein, P. and Le Pape, A., “Numerical simulation of hovering S-76 helicopter rotor including farfield analysis”, Paper AIAA 2016-0034, 54th AIAA Aerospace Sciences Meeting, AIAA SciTech Forum, San Diego, CA, January 4-8, 2016.
doi: 10.2514/6.2016-0034

³Min, B.-Y., Reimann, C. A., Wake, B., Jee, S. K., and Baeder, J. D., “Hovering Rotor Simulation using OVERFLOW with Improved Turbulence Model”, Paper AIAA 2018-1779, 56th AIAA Aerospace Sciences Meeting, AIAA SciTech Forum, Kissimmee, FL, January 8-12, 2018.
doi: 10.2514/6.2018-1779

⁴Sheng, C., Zhao, Q., and Hill, M., “Investigations of XV-15 Rotor Hover Performance and Flow Field Using U2NCLE and HELIOS Codes”, Paper AIAA 2016-0303, 54th AIAA Aerospace Sciences Meeting, AIAA SciTech Forum, San Diego, CA, January 4-8, 2016.
doi:10.2514/6.2016-0303

⁵Coder, J. G., “OVERFLOW Rotor Hover Simulations Using Advanced Turbulence and Transition Modeling”, Paper AIAA 2017-1432, 55th AIAA Aerospace Sciences Meeting, AIAA SciTech Forum, Grapevine, TX, January 9-13, 2017.
doi: 10.2514/6.2017-1432

⁶Sheng, C., Wang, J., and Zhao, Q., “Improved Rotor Hover Predictions Using Advanced Turbulence Modeling”, *Journal of Aircraft*, Vol. 53, (5), 2016, pp. 1549-1560.
doi:10.2514/1.C033512

⁷Vieira, B. A., Kinzel, M. P, and Maughmer, M. D., “CFD Hover Predictions Including Boundary-Layer Transition”, Paper AIAA 2017-1665, 55th AIAA Aerospace Sciences Meeting, AIAA SciTech Forum, Grapevine, TX, January 9-13, 2017.
doi: 10.2514/6.2017-1665

⁸Parwani, A. and Coder, J. G., “Effect of Laminar-Turbulent Transition Modeling on PSP Rotor Hover Predictions”, Paper AIAA 2018-0308, 56th AIAA Aerospace Sciences Meeting, AIAA SciTech Forum, Kissimmee, FL, January 8-12, 2018.
doi: 10.2514/6.2018-0308

⁹Zhao, Q., Wang, J., Sheng, C. “Numerical Simulations and Comparisons of PSP and S-76 Rotors in Hover”, Paper AIAA 2018-1780, 56th AIAA Aerospace Sciences Meeting, AIAA SciTech Forum, Kissimmee, FL, January 8-12, 2018.
doi: 10.2514/6.2018-1780

¹⁰Overmeyer, A. D. and Martin, P. B., “Measured boundary-layer transition and Rotor Hover Performance at Model Scale”, Paper AIAA 2017-1872, 55th AIAA Aerospace Sciences Meeting, Grapevine, TX, 2017.
doi: 10.2514/6.2017-1872

¹¹Weiss, A., Gardner, A. D., and Klein, C., “Boundary-layer transition measurements on Mach-scaled helicopter rotor blades in climb”, *CEAS Aeronautical Journal*, Vol. 8, (4), 2017.
doi: 10.1007/s13272-017-0263-2

¹²Schwermer, T., Gardner, A.D., and Raffel, M., “A novel experiment to understand the dynamic stall phenomenon in rotor axial flight”, *Journal of the American Helicopter Society*, Vol. 64, (1), 2019.
doi: 10.4050/JAHS.64.012004

¹³Letzgus, J., Gardner, A. D., Schwermer, T., Keßler, M., and Krämer, E., “Numerical investigations of Dynamic Stall on a Rotor with Cyclic Pitch Control”, *Journal of the American Helicopter Society*, Vol. 64, (1), 2019.
doi: 10.4050/JAHS.64.012007

¹⁴Heister, C., “Semi-/empirical transition prediction and application to an isolated rotor in hover”, *Int. J. Engineering*

Systems Modelling and Simulation, Vol. 4, (1/2), 2012.
doi: 10.1504/IJESMS.2012.044845

¹⁵Richez, F. Nazarians, A., and Lienard, C., “Assessment of laminar-turbulent transition modeling methods for the prediction of helicopter rotor performance”, 43rd European Rotorcraft Forum, Milan, Italy, September 12-15, 2017

¹⁶Heister, C. C., “A Method for Approximate Prediction of Laminar-Turbulent Transition on Helicopter Rotors”, Journal of the American Helicopter Society, Vol. 63, (3), 2018, pp. 1-14.
doi: 10.4050/JAHS.63.032008

¹⁷Raffel, M., De Gregorio, F., de Groot, K., Schneider, O., Sheng, W., Gibertini, G., and Seraudie, A., “On the generation of a helicopter aerodynamic database.”, Aeronautical Journal, Vol. 115, (1164), 2011, pp. 103-112.
doi: 10.1017/S0001924000005492

¹⁸Pahlke, K., “The GOAHEAD Project”, 33rd European Rotorcraft Forum, Kazan, Russia, September 11-13, 2007.

¹⁹Schwarz, Th. and Pahlke, K., “CFD Code Validation for Complete Helicopters-The European GOAHEAD Project”, American Helicopter Society 67th Annual Forum, Virginia Beach, VA, May 3-5, 2011.

²⁰Langtry, R. B. and Menter, F. R., “Correlation-Based Transition Modeling for Unstructured Parallelized Computational Fluid Dynamics Codes”, *AIAA Journal*, Vol. 47, (12), 2009, pp. 2894-2906.
doi: 10.2514/1.42362.

²¹Shaw, S. T., Hill, J. L., and Qin, N., “Application of Engineering Transition Models to an Isolated Helicopter Rotor in Hovering Flight,” Paper AIAA 2005-467, 43rd AIAA Aerospace Sciences Meeting & Exhibit, Reno, NV, January 10-13, 2005.
doi: 10.2514/6.2005-467

²²Zografakis, G., Barakos, G., and Johnson, M., “Transition Modelling for Rotorcraft CFD”, 34th European Rotorcraft Forum, Liverpool, UK, September 16-19, 2008.

²³Weiss, A., Gardner, A. D., Schwermer, T., Klein, C., and Raffel, M., “On the Effect of Rotational Forces on Rotor Blade Boundary-Layer Transition”, *AIAA Journal*, Vol. 57, (1), 2019.
doi: 10.2514/1.J057036

²⁴Gardner, A.D. and Richter, K., “Boundary-layer transition determination for periodic and static flows using phase-averaged pressure data”, *Experiments in Fluids*, Vol. 56, (6), 2015.
doi: 10.1007/s00348-015-1992-9

²⁵Cambier, L., Heib, S., and Plot, S., “The ONERA elsA CFD software: input from research and feedback from industry”, *Mechanics & Industry*, Vol. 14, (3), 2013, pp. 159-174.
doi: 10.1051/meca/2013056

²⁶Menter, F. R., “Two-equation eddy-viscosity transport turbulence model for engineering applications”, *AIAA Journal*,

Vol. 32, (8), 1994, pp. 2066-2072.
doi: 10.2514/3.12149

²⁷Cliquet, J., Houdeville, R., and D. Arnal, “Application of Laminar-Turbulent Transition Criteria in Navier-Stokes Computations”, *AIAA Journal*, Vol. 46, (5), 2008, pp. 1182-1190.
doi: 10.2514/1.30215

²⁸Perraud, J., Deniau, H., and Casalis G., “Overview of transition prediction tools in the elsA software”, 11th World Congress on Computational Mechanics, Barcelona, Spain, July 20 - 25, 2014.

²⁹Schwamborn, D., Gerhold, T., and Heinrich, R., “The DLR TAU-Code: Recent Applications in Research and Industry,” Paper No. 619, European Conference on Computational Fluid Dynamics ECCOMAS, Egmond aan Zee, Netherlands, September 5-8, 2006.

³⁰Arnal, D., “Three-Dimensional Boundary Layers: laminar-Turbulent Transition”, AGARD Report No. 741, Toulouse Cedex, France, 1987.

³¹Mayle, R. E., “The Role of Laminar-Turbulent Transition in Gas Turbine Engines”, *ASME Journal of Turbomachinery*, Vol. 113, (4), 1991, pp. 509-537.
doi: 10.1115/1.2929110

³²Poll, D. I. A., “Some Aspects of the Flow Near a Swept Attachment Line with Particular Reference to boundary-layer transition”, Cranfield Institute of Technology-Report No. 7805, 1978.

³³Drela, M., “A User’s Guide to MSES 3.05”, Massachusetts Inst. of Technology, Cambridge, MA, July 2007,

³⁴Schrauf, G., “COCO-A Program to Compute Velocity and Temperature Profiles for Local and Nonlocal Stability Analysis of Compressible, Conical Boundary Layers with Suction,” Zentrum für angewandte Raumfahrttechnologie und Mikrogravitation (ZARM) TR, Bremen, Germany, 1998.

³⁵Schrauf, G., “LILO 2.1-Users Guide and Tutorial”, GSSC TR 6, Bremen, Germany, 2006.

³⁶Spalart, P. R. and C. L. Rumsey, “Effective inflow conditions for turbulence models in aerodynamic calculations”, *AIAA Journal*, Vol. 45, (10), 2007, pp.2544-2553.
doi: 10.2514/1.29373

³⁷Schlichting, H. and Gersten, K., *Grenzschicht-Theorie*, 10th ed., Springer, Berlin, Germany, 2006.

³⁸Mertens, C., Wolf, C. C., and Gardner, A. D., “Unsteady boundary-layer transition detection with local infrared thermography”, STAB 2018, Darmstadt, Germany, November 6-7, 2018.

³⁹Weiss, A., Wolf, C. C., Braukmann, J. N, Raffel, M., and Heineck, J. T., “Unsteady boundary-layer transition measurements on a rotating blade at cyclic pitch using differential infrared thermography”, Abstract submitted to 45th European Rotorcraft Forum, Warsaw, Poland, September 17-19, 2019.